Magnetic Resonance in Medicine 53:1372–1382 (2005)

Optimizing Spatiotemporal Sampling for *k-t* BLAST and *k-t* SENSE: Application to High-Resolution Real-Time Cardiac Steady-State Free Precession

Jeffrey Tsao,[1]* Sebastian Kozerke,[1] Peter Boesiger,[1] and Klaas P. Pruessmann[1]

In *k-t* BLAST and *k-t* SENSE, data acquisition is accelerated by sparsely sampling *k*-space over time. This undersampling in *k-t* space causes the object signals to be convolved with a point spread function in *x-f* space (*x* = spatial position, *f* = temporal frequency). The resulting aliasing is resolved by exploiting spatiotemporal correlations within the data. In general, reconstruction accuracy can be improved by controlling the *k-t* sampling pattern to minimize signal overlap in *x-f* space. In this work, we describe an approach to obtain generally favorable patterns for typical image series without specific knowledge of the image series itself. These optimized sampling patterns were applied to free-breathing, untriggered (i.e., real-time) cardiac imaging with steady-state free precession (SSFP). Eddy-current artifacts, which are otherwise increased drastically in SSFP by the undersampling, were minimized using alternating *k*-space sweeps. With the synergistic combination of the *k-t* approach with optimized sampling and SSFP with alternating *k*-space sweeps, it was possible to achieve a high signal-to-noise ratio, high contrast, and high spatiotemporal resolutions, while achieving substantial immunity against eddy currents. Cardiac images are shown, demonstrating excellent image quality and an in-plane resolution of ~2.0 mm at >25 frames/s, using one or more receiver coils. Magn Reson Med 53:1372–1382, 2005.

Key words: MRI; *k-t* BLAST/*k-t* SENSE; SSFP; parallel imaging; prior-information-driven dynamic imaging

In dynamic MR imaging, there is a tradeoff between the achievable spatial and temporal resolutions. For example, to achieve a higher spatial resolution, more time is needed to acquire data for each time frame, so the images are updated less frequently. In order to relax the tradeoff between spatial and temporal resolutions, various strategies have been applied to make the acquisition process more efficient. Toward this direction, there has been increasing interest in exploiting spatiotemporal correlation to enhance resolution in dynamic MR imaging. This trend is reflected in the development of several methods, such as UNaliasing by Fourier-encoding the Overlaps using the temporaL Dimension (UNFOLD) (1), SENSitivity Encoding incorporating Temporal filtering (TSENSE) (2), and *k-t* BLAST (Broad-use Linear Acquisition Speed-up Technique) (3) and *k-t* SENSE (SENSitivity Encoding) (3). These techniques are based on the observation that data points in dynamic images are not mutually independent, but they usually exhibit a high degree of correlation, both in the temporal and in the spatial dimensions. Hence, based on knowledge or models of this correlation, it is feasible to acquire only a reduced amount of data and recover the missing portion afterward. The extent of data reduction is referred to as the acceleration factor hereafter, as denoted by *R*.

The distinctive feature of *k-t* BLAST is that it has the capacity to account specifically for the actual correlation present in a given data set. This is achieved by learning the correlation in a training stage and utilizing this knowledge as an estimate of the signal covariance within the data space. *k-t* SENSE is similar to *k-t* BLAST, but it additionally takes into account the spatial encoding effect of coil sensitivity, if multiple receiver coils are used for signal reception. It should be noted that for *k-t* BLAST and *k-t* SENSE, only a portion of *k*-space is refreshed at each time frame, while the remaining data are estimated based on minimizing the expected least squares error. An important characteristic of the reconstruction procedure is that the reconstructed images are guaranteed to be consistent with the acquired data. Moreover, unlike alternative techniques such as view sharing, it does not implicitly restrict or attenuate any temporal frequencies (except for frequencies that overlap with the direct-current component) (3). The temporal frequencies are simply traded off among one another on a voxel-by-voxel basis, based on the estimated image content. Therefore, the frame rate reconstructed by *k-t* BLAST and *k-t* SENSE reflects the true highest recoverable temporal frequency, although the amount of signals found at that temporal frequency is entirely dependent on the image contents.

The details of *k-t* BLAST and *k-t* SENSE have been described earlier in Ref. (3). Briefly, raw data are sampled sparsely in *k*-space over time *t* (referred to as *k-t* space (4) hereafter). As a result, the object signals are replicated in the reciprocal *x-f* space (3,5), potentially leading to undesirable signal overlap (i.e., aliasing). *x-f* space is related to *k-t* space by an inverse Fourier transform (Fig. 1). "*x*" and "*f*" refer to spatial position and temporal frequency, respectively. Here, "*x*" represents a general spatial position, so it also stands for "*y*" to "*z*" in the same manner that "*k*" stands for "k_x, " "k_y," or "k_z". The aliasing between the signal replicates in *x-f* space is then resolved using signal covariance learned from low-resolution training data. In general, reconstruction accuracy is improved if there is as little aliasing as possible, since there will be fewer over-

[1]Institute for Biomedical Engineering, University of Zurich and Swiss Federal Institute of Technology (ETH) Zurich, Zurich, Switzerland.

Grant sponsor: SEP program of the ETH Zurich; Grant number: TH7/02–2; Grant sponsor: Canadian Institutes for Health Research.

*Correspondence to: Jeffrey Tsao, Novartis Institutes for BioMedical Research, Inc., Central Technologies, MRI, 250 Massachusetts Avenue, Cambridge, MA 02446, USA. E-mail: jeffrey.tsao@pharma.novartis.com.

Received 2 March 2004; revised 17 December 2004; accepted 28 December 2004.

DOI 10.1002/mrm.20483
Published online in Wiley InterScience (www.interscience.wiley.com).

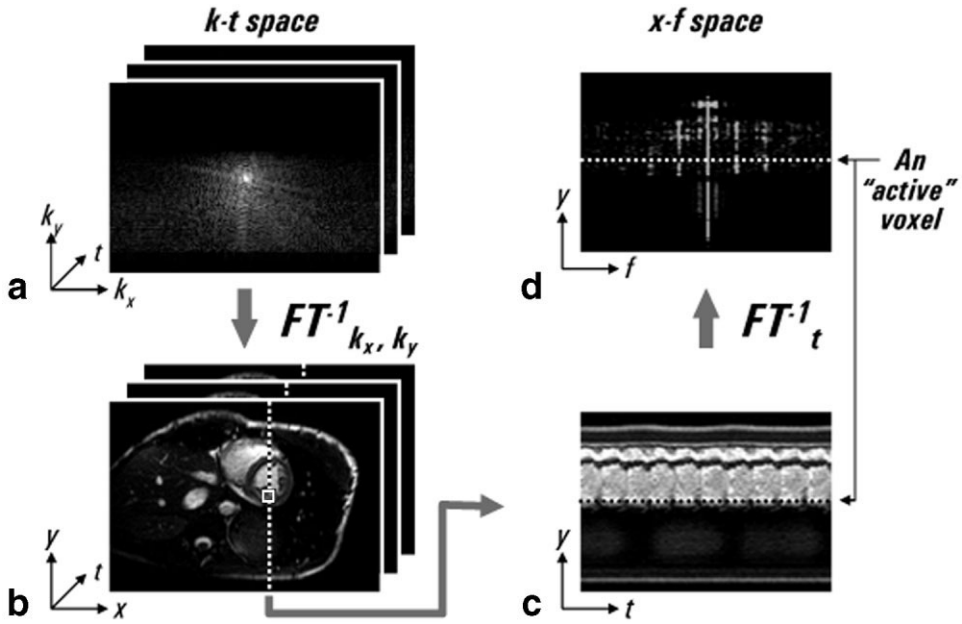

FIG. 1. Relationship among various linear spaces for a typical time series of fully sampled real-time SSFP cardiac images (see Table 1 for acquisition parameters). (**a**) A time series of *k*-space data. The black regions at the top and bottom indicate the omitted portions of *k*-space to speed up acquisition (from partial-Fourier acquisition and zero-filling). These omitted regions cause a slight spatial broadening of the point spread function, which is otherwise unchanged. Applying inverse Fourier transform to the k_x and k_y axes yields a time series of images (**b**). The profile at one frequency-encoded position *x* at different time *t* is shown in (**c**). The position of the profile is indicated by dashed line in (b). Applying inverse Fourier transform along time *t* yields the *x-f* space representation (**d**), where *x* denotes a general spatial position (i.e., represented by *y* in this case) and *f* denotes temporal frequency. An example of an active voxels is indicated by horizontal dotted lines in (c) and (d), and its position is indicated by a white square in (b).

lapped signals to separate, and inaccuracies in the estimated signal covariance become less consequential.

The amount of signal overlap in *x-f* space depends on the point spread function, which in turn depends on the sampling pattern in *k-t* space. It should be noted that this point spread function is in both space and temporal frequency (i.e., in *x-f* space). Since there are regions in *x-f* space that are essentially empty (Fig. 1d), it is possible to change the effective amount of signal overlap by controlling the *k-t* sampling pattern judiciously. The purpose of this work was to find *k-t* sampling patterns that are near-optimal for typical image series, without using specific knowledge about the image series itself. The resulting sampling patterns are important, since they can be determined a priori, thus obviating the need to adapt the acquisition on-line to the object being imaged.

We demonstrate the utility of these optimized sampling patterns for *k-t* BLAST and *k-t* SENSE in free-breathing, untriggered (referred to as real-time hereafter) cardiac imaging with the steady-state free-precession (SSFP) sequence (6). SSFP has become an indispensable sequence (7) for functional assessment of the heart, due to its improved blood-to-myocardium contrast and higher signal-to-noise ratio (SNR), compared to spoiled steady-state sequences, such as Fast Low-Angle SHot (FLASH) (8). However, SSFP is susceptible to system instabilities, such as eddy currents. This susceptibility is particularly problematic at the higher acceleration factors achievable by *k-t* BLAST and *k-t* SENSE. This is because the enlarged jumps in *k*-space resulting from sparse sampling lead to drastically amplified eddy-current-related artifacts. In this work, the eddy-current effects were reduced by traversing through *k-t* space in a smoother fashion with alternating sweeps (9). By combining SSFP with *k-t* BLAST and *k-t* SENSE while controlling eddy currents, it was feasible to achieve high spatial (~2.0 mm) and temporal (>25 frames/s) resolutions in real-time cardiac SSFP imaging, with excellent image quality.

THEORY

Lattice Sampling in *k-t* Space and Point Spread Function in *x-f* Space

In dynamic imaging, the raw data are acquired in *k-t* space (4) (i.e., *k*-space at different time points *t*). In general, *k-t* space can be sampled in any pattern that is physically realizable within the constraints (i.e., maximum strength and slew rate) of the gradient system. In this work, we restrict the sampling pattern to conform to a lattice (10,11) (i.e., a sheared grid), where the nodes of the lattice represent the sampled points in *k-t* space. The advantage of using a lattice sampling pattern is that the corresponding point spread function is also a lattice (Fig. 2), which simplifies the reconstruction significantly (3). Since only a finite portion of *k-t* space is sampled, the point spread function is strictly speaking a convolution between a lattice and a sinc function (Fig. 2, bottom left). The main lobes of these superposed sinc functions indicate the locations in *x-f* space from where most of the aliasing originates. The use of lattices naturally suggests rectilinear sampling of *k*-space (12). Since the frequency-encoding

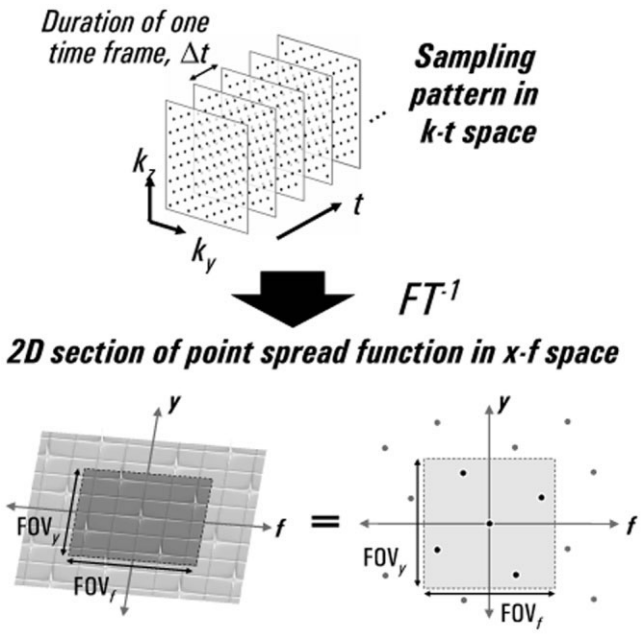

FIG. 2. (**Top**) *k-t* sampling pattern. Data are assumed to be acquired at discrete time frames, separated by Δt. Applying inverse Fourier transform to the *k-t* sampling pattern yields the point spread function in *x-f* space. (**Bottom**) Only a 2D section of the point spread function is displayed. A surface rendering of the point spread function, which is a convolution between a lattice and a since function, is shown on the left. A simplified representation is shown on the right, where the dots indicate the sinc-shaped main lobes of the point spread function. The gray square indicates the field of view. Due to the lattice structure of the *k-t* sampling pattern, the *x-f* point spread function is also a lattice.

axis is fully sampled, this axis can be reconstructed in a straightforward manner by inverse Fourier transform. As a result, it is only necessary to consider which phase-encoding lines to acquire at each time point, so the sampling problem is reduced in complexity by one dimension. In general, choosing the sampling pattern itself or the corresponding point spread function is equivalent, since the two are related (Fig. 2). In this case, it is simpler to find the solution if we consider the latter.

Criteria for Choosing the Point Spread Function

To minimize signal overlap in *x-f* space, the main lobes of the point spread function should be arranged such that positions containing large signals in *x-f* space overlap with positions containing very little signal. Any given sampling pattern will not be optimal for all image series, since it depends on the actual signal distribution of the object being imaged. Nevertheless, it is possible to choose sampling patterns that are generally favorable by exploiting four characteristics of typical image series. First, the autocorrelation among voxel intensities typically decreases with increasing distance (13). In other words, far-apart voxels tend to be less similar. Second, the signal magnitude tends to be lower at higher temporal frequencies (14) (see right and left edges of *x-f* space in Fig. 1d). Third, multiple regions within an image often remain stationary or they move in a coherent fashion, as a result of bulk motion (e.g., respiration and heart beat). Therefore, these regions contain significant signals at similar temporal frequencies. Fourth, there may be certain "active" voxels, where the intensities vary significantly over time, thus requiring many temporal frequency components for accurate representation. Figure 1 illustrates an example of an active voxel (indicated by dotted lines on the right), which undergoes significant temporal variations.

The first two considerations suggest that if we have an *x-f* position with considerable signal, it is likely that nearby *x-f* positions also contain significant signals. Therefore, to minimize signal overlap, the main lobes of the point spread function should be separated as far as possible in *x-f* space. The third and fourth considerations suggest that it is preferable to have the point-spread-function main lobes within the field of view situated at different temporal frequencies and at different spatial positions. In this way, signal overlap is minimized among image regions that share similar temporal frequencies, and any active voxel is prevented from overlapping with itself. It should be noted that if multiple receiver coils are used for signal reception, the knowledge of coil sensitivities (15) can aid in resolving the aliasing even if the signals originate from the same frequency (e.g., with *k-t* SENSE (3)). However, since this situation is similar to setting too small a field of view along the spatial axes, we will not consider it in the subsequent analysis. These four considerations are the selection criteria for choosing favorable point spread functions below.

Choosing the Point Spread Function

We begin by defining a target temporal resolution Δt, which is user-defined in an analogous fashion to the target spatial resolution. This temporal resolution Δt is chosen based on two tradeoffs. On the one hand, Δt should be short enough relative to the time scale of the motion being observed. On the other hand, it should be long enough so that the training acquisition can collect sufficient *k*-space data to roughly depict the object during one Δt. For real-time cardiac imaging, Δt is typically chosen to be ~33 ms, thus yielding a frame rate of ~30 frames/s. This duration Δt is sufficient to acquire approximately 10 phase-encode lines (16) using FLASH- or SSFP-type sequences, where one phase-encode line is acquired in a repetition time (TR) of ~3 ms. As a result, this allows the training acquisition to resolve image details on the order of 1/10 the field of view.

The phase-encode lines acquired within each Δt are considered to be from the same time frame (3,5) (Fig. 2), even though they are actually acquired at slightly different time instances. This assumption leads to a slight warp of the sampling lattice, which can generally be ignored if the warp is sufficiently small. The reciprocal of Δt determines the maximum frame rate FOV_f that is resolved (Fig. 2):

$$\mathrm{FOV}_f = 1/\Delta t. \qquad [1]$$

Since *k-t* space is sampled at an interval of Δt, the point spread function in *x-f* space is implicitly periodic with a period of FOV_f along the temporal frequency axis *f*.

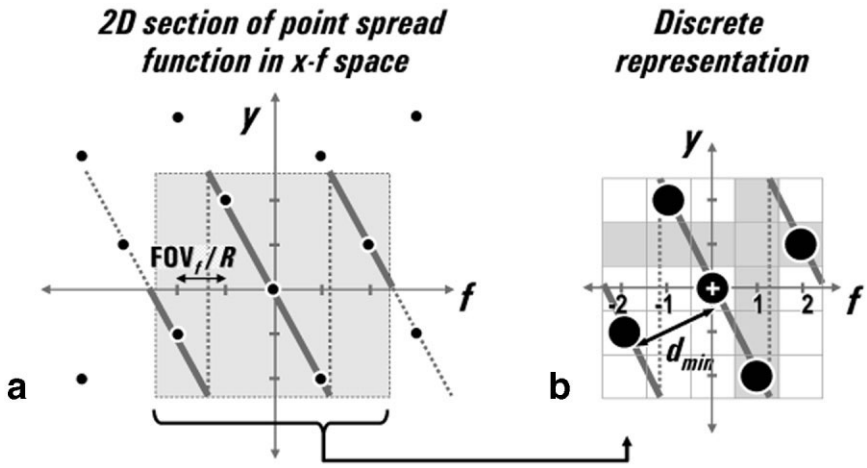

FIG. 3. (**a**) A 2D section of the point spread function in *x-f* space. The dots indicate the sinc-shaped main lobes of the point spread function. The gray square indicates the field of view. All the main lobes lie on a periodically wrapped line (see thick gray line), and they are situated at uniformly spaced locations along each axis as indicated by the tick marks. As a result, the problem of choosing the main-lobe locations can be converted to a discrete problem (**b**), where the locations of the main lobes are confined to a square array. One of the main lobe has to be at the origin, marked by the white "+". The second main lobe can be chosen to be situated at one of the gray squares. $d_{\min}$ indicates the minimum separation distance among the main lobes.

To simplify the problem of choosing the point spread function, we assume that *k*-space is uniformly discretized and we can only sample points at the discretized positions. This is similar to the typical situation with Cartesian sampling, where all the phase-encode positions are multiples of a phase-encode step size. For 2D sampling, this assumption actually has no effect, since the periodicity of the lattice automatically ensures that all the sampled positions will always fit onto a uniformly discretized grid. The assumption only affects 3D sampling, but the restriction is rather mild, since any 3D sampling lattice can be well approximated by a sufficiently fine discretization. For further simplification, we assume that the discretization steps along k_y and k_z correspond to the reciprocal of the field of view, in the same fashion as for usual Cartesian sampling. This choice does not limit the generality of the present approach, since choosing another step size is equivalent to choosing a different field of view, as discussed further below.

At this point, we have assumed that *k-t* space is uniformly discretized along the *t* axis as well as along the *k* axes. Thus, the point spread function in *x-f* space is periodic along the temporal frequency axis as well as along the spatial axes. The periodicity confines all the main lobes within the field of view to lie on a straight line that is periodically wrapped (see thick gray line in Fig. 3a). Also, the main lobes can only be situated at a set of uniformly distributed positions along the spatial and temporal frequency axes (as indicated by the tick marks on the axes of Fig. 3a). These positions are separated by a distance equal to the field of view divided by the acceleration factor *R* (Fig. 3a). It should be noted that while the main lobes are always situated at one of these positions, they may not occupy all of the positions. In that case, the main lobes are separated by a distance farther than $1/R$ of the field of view along that particular axis. From Fig. 3a, it can be seen that the periodicity in the geometric arrangement implicitly restricts *R* to be integer-valued. If a fractional *R* is desired, one would simply choose the point spread function for the next higher integer-valued *R* and increase the FOV by the corresponding amount. Since the main lobes can only be situated at these discrete positions, the problem of choosing the point spread function in a continuous *x-f* space can now be converted to a discrete selection problem (see Fig. 3b), which is significantly simpler to solve.

In the discrete case (Fig. 3b), one defines an $R \times R$ array in 2D or an $R \times R \times R$ array in 3D to represent a discretized *x-f* space. The first main lobe is placed at the origin (see "+" in Fig. 3b). The problem is to choose where to place the second main lobe, which should be located somewhere at $f = 1$, $y = 1$, or $z = 1$. There are only limited possibilities to choose from (see shaded squares in Fig. 3b), and the number of possibilities can be further reduced by noting the symmetry of the problem. After choosing a location for the second main lobe, the locations of the remaining main lobes are automatically fixed, since they all lie on a periodically wrapped line (see thick gray line in Fig. 3b). The resulting point spread function is only feasible if all the main lobes are situated at different spatial positions and at different temporal frequencies. One can then search through all feasible point spread functions to find the ones that maximize the minimum separation distance among the main lobes (see $d_{\min}$ in Fig. 3b). It should be noted that the distances along the spatial axis and the temporal frequency axis are normalized with respect to the corresponding field of view (FOV_y and FOV_f) so that they can be compared on an equal footing. Once the point spread function is chosen, it can be Fourier transformed to yield a section of the *k-t* sampling pattern with a size of $R \times R$ in 2D and $R \times R \times R$ in 3D. The full *k-t* sampling pattern is a periodic replication of this section.

The discrete selection procedure just described has the advantage that it is efficient to evaluate all feasible point spread functions to achieve a global optimization. By maximizing the main-lobe separation distance $d_{\min}$, one automatically searches for the most isotropic lattice. Further-

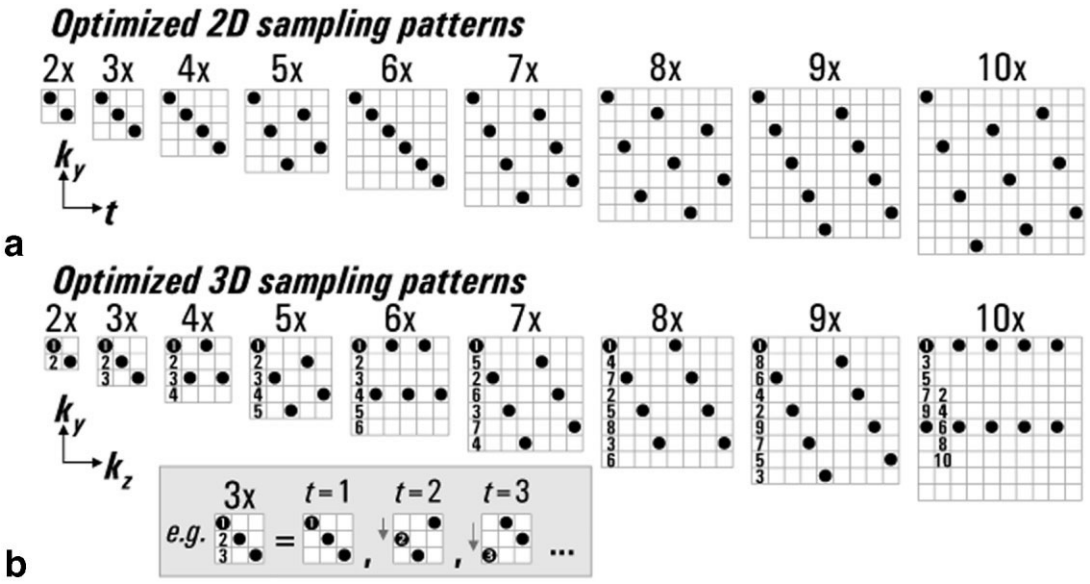

FIG. 4. Optimized *k-t* sampling patterns in (**a**) 2D and in (**b**) 3D for acceleration factors *R* up to 10×. Note that these sampling patterns are optimized for a given discrete step size in *k*-space, so the net acceleration factor may be different if a different step size is used. See text for details. In each $R \times R$ array, the black dots indicate the sampled positions. The overall *k-t* sampling pattern is a periodic extension of this array. For the 3D patterns, the sampling pattern at time point 1 is displayed. The sampling patterns at other time points (as indicated by the inset numbers) are shifted versions of the displayed patterns (see bottom as an example, gray arrows indicate shift).

more, the discrete array itself indicates the minimum number of discrete steps needed to be acquired along the *k* and *t* axes. For example, if the main lobes are situated at *M* of the *R* discrete positions along the temporal frequency (*f*) axis, it is necessary to acquire at least *M* time frames. This is to ensure that the half width of the point spread function main lobes is at least as narrow as the main-lobe separation distance along the *f* axis. This is the absolute minimum, but in general, it is advisable to have more than the minimum number of time frames (e.g., $3 \times M$) to ensure adequate signal separation. The same consideration applies to the *y* and *z* axes in determining the minimum number of k_y and k_z phase encode lines to acquire, respectively.

Optimized Sampling Patterns

Figure 4 shows examples of optimized sampling patterns in 2D and 3D for various acceleration factors *R*. These patterns were derived by the exhaustive but efficient search procedure described above. For each *R*, there are multiple point spread functions that can achieve the same $d_{\min}$. Such point spread functions are related to one another by symmetry or rotation. One may choose among these equivalent point spread functions arbitrarily or based on the actual or estimated signal distribution of the object. To avoid visual clutter, only an $R \times R$ section of the 2D sampling patterns is shown, with the axes corresponding to k_y and time *t* (Fig. 4a). For 3D patterns, only an $R \times R$ section at a particular time point is shown, with the axes corresponding to k_y and k_z (Fig. 4b). The sampling patterns at other time points are obtained by shifting the displayed pattern (see example at bottom of Fig. 4b). The numbers in the diagram indicate the shifted position of one point in the sampling pattern at the noted time frames.

Figure 5 shows the minimum main-lobe separation distance $d_{\min}$ for the optimized patterns in both 2D and 3D. In general, 3D patterns have a larger separation distance $d_{\min}$ than 2D patterns, since *x-f* space has an additional dimension for separating the main lobes. The optimized sampling patterns tend to distribute the main lobes as uniformly as possible in all regions of *x-f* space in order to maximize $d_{\min}$. Hence, they approach the shape of a simplex-based grid, i.e., a triangular lattice in 2D and a tetragonal lattice in 3D. Simplex-based lattices are solutions to the so-called sphere-packing problem (17), so they maximize the separation distance among the lattice nodes packed inside an *x-f* space of a given size. The reason that

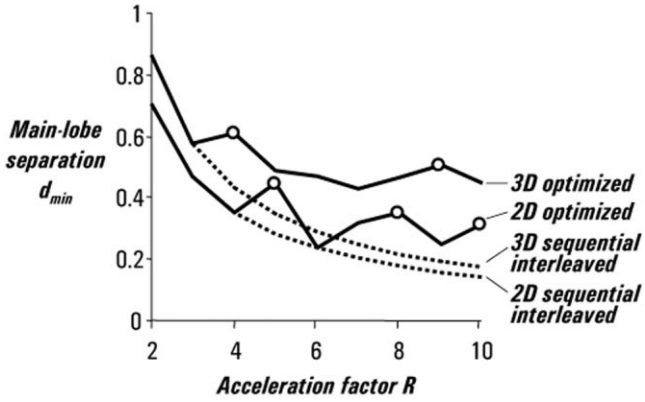

FIG. 5. Minimum main-lobe separation distance $d_{\min}$ at different acceleration factors *R* for optimized lattices (solid line) or sequential interleaved lattices (dotted line) in both 2D and 3D. Favorable acceleration factors are indicated by white circles, where the main-lobe separation is particularly larger for the optimized lattice, thus minimizing potential signal overlap. The separation distance is generally larger for the 3D patterns than for the 2D patterns due to the additional dimension in *x-f* space.

Table 1
Acquisition Parameters

	SENSE 2.5×(Fig. 1)	Sampling pattern (Fig. 7)	Eddy currents (Fig. 8)	Short-axis view (Fig. 9a, b)	Four-chamber view (Fig. 9c, d)
FOV (mm × mm)	320 × 240	320 × 272	320 × 304	320 × 224	320 × 304
Slice thickness (mm)	8	8	8	8	8
No. phase-encoding lines per time frame	25	10	160	9	11
No. frequency-encoding points	160	160	160	208	160
TE (ms)/TR (ms)	1.62/3.70	1.65/3.30	1.41/2.80	1.85/3.70	1.49/3.00
Flip angle	60°	60°	60°	60°	60°
Partial Fourier	66%	60%	No	66%	64%
Raw frame rate (frames/s)	10.8	30.3	2.2	30.0	30.3
Filtered frame rate (frames/s)	—	27.2	—	27.1	27.2
In-plane resolution (mm × mm)	2.00 × 2.53	2.00 × 2.05	2.00 × 1.90	1.54 × 2.06	2.00 × 2.22

we do not simply use simplex-based lattices and avoid the entire search procedure is mainly pragmatic, since it is somewhat difficult to ensure that the simplex-based grids fulfill the four considerations mentioned above, particularly for higher dimensional grids.

In contrast to the optimized patterns, the worst sampling patterns place all the main lobes along the diagonal in *x-f* space. The corresponding *k-t* sampling pattern is a sequential interleaved pattern. At certain acceleration factors, the sequential interleaved pattern is the only available choice (e.g., for $R = 2$ or 3 in 2D and 3D; see Fig. 4). For this sampling pattern, the separation distance $d_{\min}$ decreases as $\sqrt{2}/R$ in 2D or as $\sqrt{3}/R$ in 3D. By using an optimized sampling pattern, $d_{\min}$ can increase significantly, particularly at higher acceleration factors, thereby reducing the potential amount of signal overlap. Figure 5 reveals that several acceleration factors are particularly favorable, since they allow further separation of the main lobes. These are indicated by the local maxima of the curves (Fig. 5). They include 5-, 8-, and 10-fold acceleration in 2D and 4- and 9-fold acceleration in 3D (see white circles in Fig. 5). It is important to note that these sampling patterns are optimized based on a fixed discrete step size in *k*-space. In general, one also has the freedom to alter the step size by choosing a different field of view, as described further in the Discussion.

Eddy Current and SSFP

In SSFP imaging, eddy-current problems arise when successive phase encodes differ by a large step in *k*-space. In the common case of 2D dynamic imaging with a linear phase-encode order, eddy-current-related artifacts are almost negligible (9), since the eddy currents generated by the phase-rewinding gradient from one TR mostly cancel those generated by the phase-encoding gradient in the next TR. Problems mainly arise when one finishes with the last phase-encode line and jumps back to the first one. Nevertheless, the artifacts are rather benign, since this happens infrequently, and the eddy currents only affect localized areas in *k*-space.

The situation changes drastically when SSFP is applied in a straightforward manner at the high acceleration factors achievable with *k-t* BLAST and *k-t* SENSE. First, the undersampling causes the end-to-end jump in *k*-space to occur more frequently (once every N/R lines versus once every N lines in the unaccelerated case). Thus, large eddy currents are generated more often, which strongly contaminate most of the acquired data, since there is insufficient time for the eddy-current-induced effects to decay. Second, the undersampling leads to larger step sizes in *k*-space, which result in more residual eddy currents at each step. In this work, the eddy-current problems were reduced by alternating the phase-encode order from one time point to the next. This eliminates the end-to-end jumps in *k*-space, which is the dominant source of eddy currents. Residual eddy-current artifacts remain due to the larger step sizes, but they are typically at a sufficiently low level to be neglected in practice.

METHODS

All data were acquired on a Philips Intera 1.5-T scanner (maximum gradient strength 30 mT/m and slew rate 150 mT/m/ms), using a five-element phased-array coil. The acquisition parameters are summarized in Table 1. The in vivo images were acquired from two healthy adults, with the phased array wrapped around the subjects' thorax. Informed consent was obtained prior to acquisition. For *k-t* SENSE, the data from all coil elements were used in reconstruction; while for *k-t* BLAST, the data from a single coil element positioned directly above the heart were used in reconstruction.

Effects of Sampling Pattern

Real-time cardiac SSFP images were acquired in the short-axis view. The data were acquired in a free-running mode at 8× acceleration using either a sequential interleaved or an optimized eightfold sampling lattice. In both cases, alternating sweep directions in *k*-space were used to reduce eddy-current problems. The acquisition parameters are summarized in Table 1. Training data were acquired with the same geometry and the same timing parameters as the undersampled data, but only the central portion of *k*-space was acquired (with the same number of phase-encode lines per time frame). Two-fold TSENSE acceleration (2) (i.e., odd or even *k*-space lines acquired at alter-

nating time frames) was used for the training data to achieve twice the spatial resolution at the same frame rate. To test the feasibility of using only a single receiver coil, an additional set of training data were acquired without TSENSE. The training and undersampled data were acquired sequentially in runs of approximately 10 s each.

Effects of Eddy Currents

Time series of 2D SSFP images were acquired from a stationary water-filled phantom. Four phase-encode orders were tested: sequential interleaved and optimized eight-fold sampling lattices, with and without alternating sweep directions in *k*-space.

Cardiac SSFP at 8× Acceleration

Real-time cardiac images were obtained in the short-axis and four-chamber views. The data were acquired in a free-running mode at 8× acceleration using an optimized lattice and alternating sweep directions in *k*-space. The acquisition procedure was the same as described above for studying the effects of the sampling pattern.

Reconstruction

Partial Fourier acquisition was used for further increases in speed in some scans (see Table 1, Fig. 1a). Unacquired *k*-space lines were filled with zeros for all partial Fourier acquisitions prior to *k-t* BLAST or *k-t* SENSE reconstruction. Acceleration resulting from partial Fourier acquisition was not included in the reported acceleration factors. The training images were reconstructed in a frame-by-frame manner. Slight low-pass temporal filtering (cut-off frequency at 90% Nyquist) was applied to the training images. For training data acquired with 2× TSENSE acceleration, this filtering improved the robustness against any residual aliasing (2), at the expense of a slightly reduced frame rate (by 10%). For training data acquired without TSENSE, this filtering was not necessary. It was implemented nonetheless so that the reconstructed images would have the same frame rate for comparison. These training images were inverse Fourier transformed along time *t*, to yield a set of low-resolution training data in *x-f* space. For the undersampled data, reconstruction was performed as described in Ref. (3).

Coil sensitivity maps, which were needed for *k-t* SENSE reconstruction, were calculated based on temporally averaged images, obtained separately for each coil and separately from the training data or the undersampled data. These images were divided by the root-mean-square image from all coils and smoothed to reduce noise. This simple method of sensitivity calibration was found to be sufficient for the in vivo images. In general. more sophisticated smoothing strategies, such as local polynomial fitting, can be used to further improve the accuracy of extracted sensitivity maps (15).

RESULTS

Effects of Sampling Pattern

Figure 6 shows the comparison between data sampled in a sequential interleaved lattice (Fig. 6a) and those sampled in an optimized lattice (Fig. 7b). For the sequential interleaved lattice (Fig. 6a), the images were contaminated by noticeable artifacts, which appeared as residual aliasing of image edges (see white arrows). Although the aliasing artifacts are unlikely to be confused with real anatomic structures, as they do not move together with the underlying structures, the appearance of these artifacts degraded image quality. Also, slightly increased blurring can be seen for fine structures such as the papillary muscles. Small features are particularly sensitive to the arrangement of the aliasing pattern, since they usually have lower signals, which are more difficult to separate. The residual aliasing and slight blurring occur in *x-f* space, and they are caused by inaccurate signal assignment, resulting from suboptimal arrangement of signal replicates and overpacking of signals in localized regions of *x-f* space. In particular, residual aliasing resulted from assigning too much signal to an *x-f* voxel, with the extra signal originating from a different source location, thereby leading to aliasing; whereas blurring resulted from assigning too little signal to an *x-f* voxel, which was therefore effectively filtered. The residual aliasing appeared as slight flickering when viewing the images as a movie, whereas blurring artifacts had a similar appearance to conventional motion blurring.

In the case of the optimized lattice, the aliasing and blurring artifacts were reduced significantly (Fig. 6b). This was because the signal replicates were separated further from one another, which resulted in less signal overlap, so signal misassignment became less problematic. In the case of *k-t* BLAST (Fig. 6b, top row), very slight residual aliasing remained in the posterior portion of the image (see open arrow). This originated from the strong signals of the fat on the anterior side and the blood in the heart. Nevertheless, it had negligible effect on image quality since it was displaced from the anatomy of interest by the point spread function. This low level of artifacts was not seen in *k-t* SENSE (Fig. 6b, bottom row), since the reconstruction was further improved with the complementary information from additional coils.

Effects of Eddy Currents

Figure 7 shows the image artifacts resulting from different ordering of the phase-encode lines. Figure 7a shows the conventional linear order, where *k*-space was sampled sequentially from one end to the next, and the process was repeated for each time point. Slight eddy currents were generated at each phase-encode step, particularly at each jump from the bottom to the top of *k*-space. Generally, for a well-tuned gradient system, these artifacts should remain small and can often be neglected, as noted by Jung et al. (9). However, as Fig. 7b shows for 8× acceleration, such artifacts were drastically amplified in the case of sparse sampling, since the end-to-end jumps occurred 8 times more frequently in that case. These jumps or discontinuities were reduced by sweeping through *k-t* space in an alternating fashion (Fig. 7c and d). With this strategy, the artifacts were eliminated in the case of full *k*-space sampling (Fig. 7c). For 8× acceleration, slight artifacts remained, since the step size from one phase-encode line to the next was still eight times larger compared to the unac-

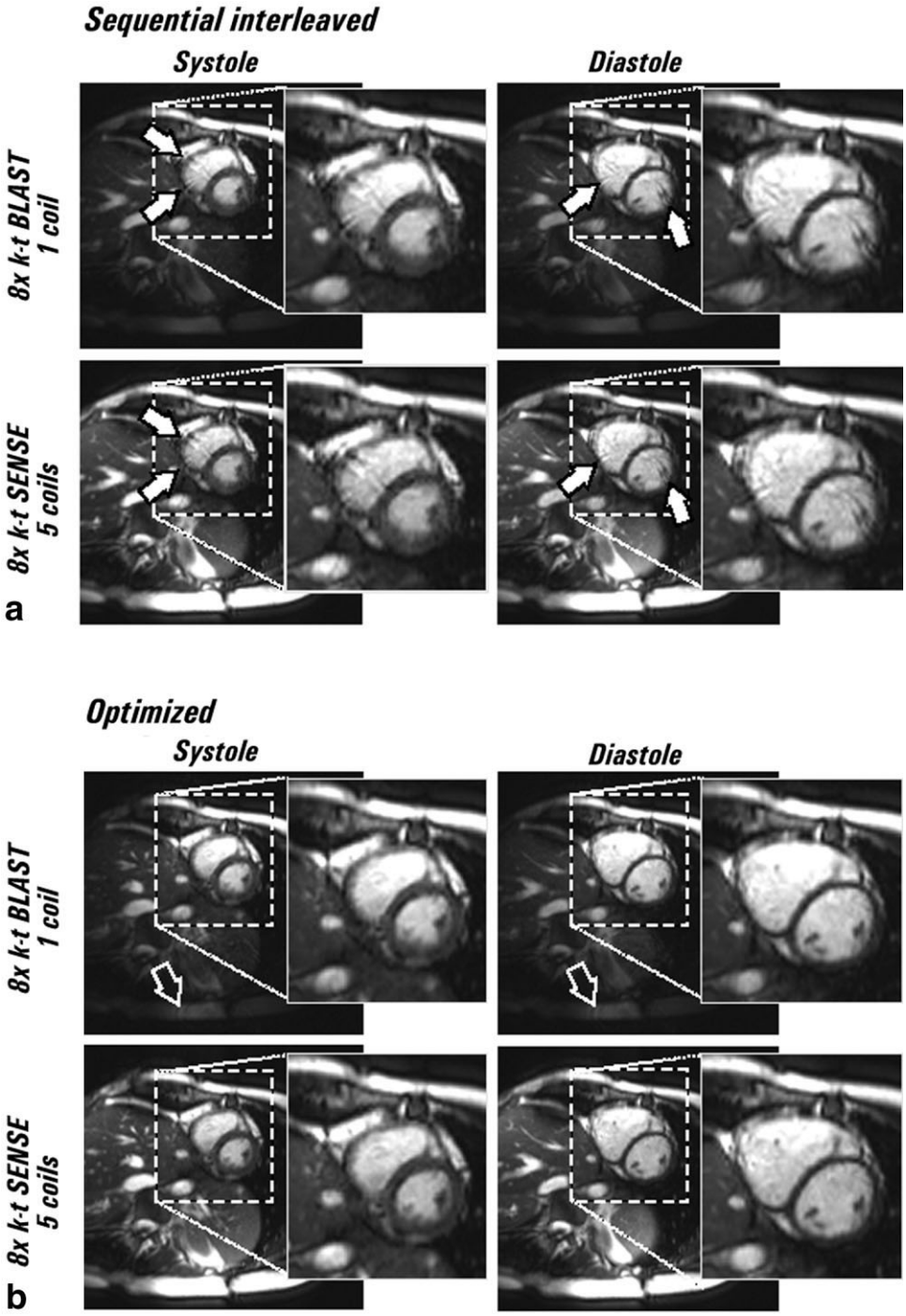

FIG. 6. The effects of sampling pattern comparing (**a**) a sequential interleaved lattice and (**b**) an optimized lattice. Short-axis images in systole and diastole are shown for *k-t* BLAST with one coil (top row) and for *k-t* SENSE with five coils (bottom row) at eightfold acceleration. For the sequential interleaved lattice (a), residual aliasing (see white arrows) and slight blurring of fine features were observed. These artifacts were significantly reduced with an optimized lattice (b). Very slight residual aliasing remained in the posterior portion of the image for *k-t* BLAST (b, top row, see open arrows), but this did not affect image quality considerably since it was displaced from the anatomy of interest by the point spread function. The residual aliasing was not observed for *k-t* SENSE.

celerated case. Nevertheless, the residual artifacts were minor and could be neglected in practice.

Cardiac SSFP at 8× Acceleration

Figure 8 shows 8× accelerated cardiac images in short-axis (Fig. 8a and b) and four-chamber views (Fig. 8c and d). Selected time frames from a single heart beat are shown. The highest recoverable temporal resolution was 27.1 frames/s and 27.2 frames/s for the short-axis and four-chamber views, respectively. Figure 8a and c show the images obtained with only one of the receiver coils, reconstructed with *k-t* BLAST. Figure 8b and d show the corresponding images obtained with five receiver coils using *k-t* SENSE. These results demonstrate the feasibility of obtaining high-quality cardiac images with high spatial and temporal resolutions, using an arbitrary number of receiver coils. Artifacts from eddy currents were not seen in any of the reconstructed images. No significant blurring or residual aliasing artifacts were observed, except in the first few and last few time frames (3), due to temporal discontinuity between those frames. This did not pose any problem, since those frames are

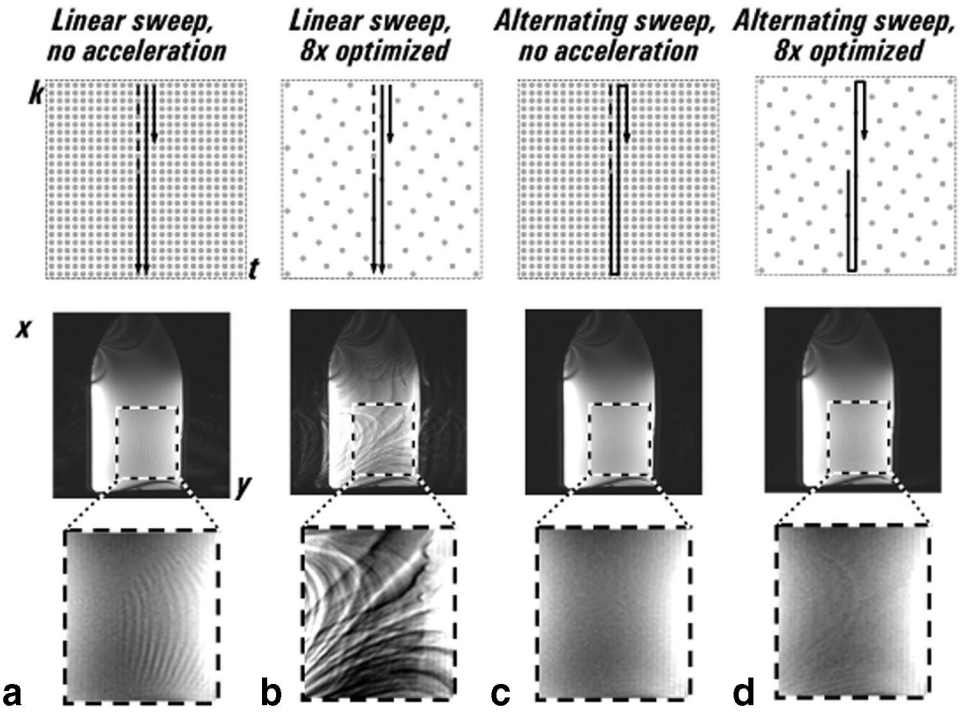

FIG. 7. Eddy-current artifacts for different ordering of the phase-encode lines in *k*-space, with and without acceleration. "*k,*" "*t,*" "*x,*" and "*y*" represent the phase-encode index, time, the frequency-encoded position, and the phase-encoded position, respectively. (**Top**) *k-t* sampling pattern with gray dots indicating sampled positions. The black arrows indicate the order of traversing *k-t* space. (**a**) A linear sweep direction (from top to bottom at every time point *t*) with full *k*-space sampling led to small but noticeable artifacts. (**b**) These artifacts were accentuated drastically when *k*-space was undersampled eightfold. (**c**) Using alternating sweeps, the artifacts were eliminated when *k*-space was fully sampled. (**d**) For eightfold undersampling with alternating sweeps, the majority of the artifacts was removed, but a slight portion remained due to reduced eddy-current compensation from the larger phase-encode step size. (c) and (d) should be compared with (a) and (b), respectively.

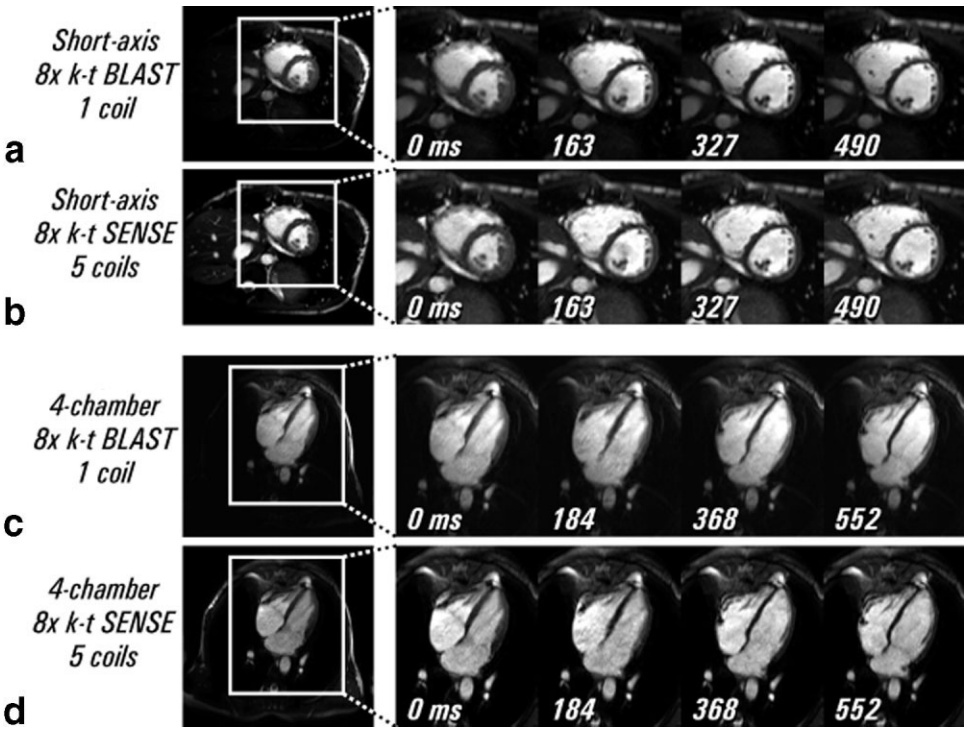

FIG. 8. Real-time cardiac SSFP images at eightfold acceleration in short-axis (**a** and **b**) and four-chamber (**c** and **d**) views. Selected time frames show the heart in different cardiac phases within a single beat. (a) and (c) show the reconstruction results with *k-t* BLAST using only the data from one coil situated above the heart. (b) and (d) show the corresponding reconstruction results with *k-t* SENSE using data from five receiver coils.

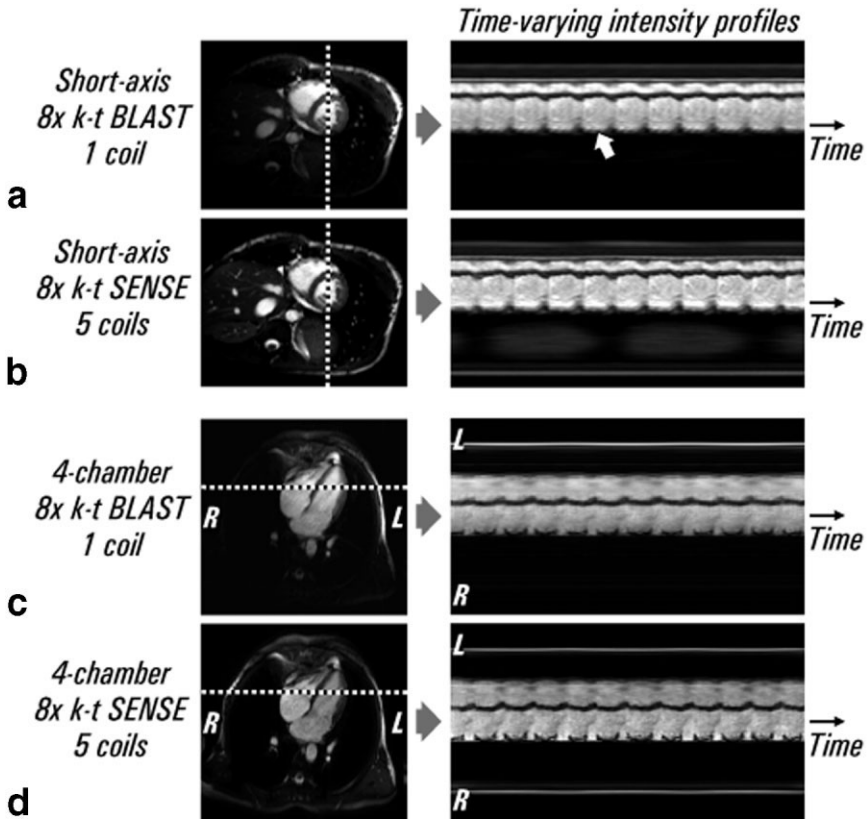

FIG. 9. The same series of real-time cardiac SSFP images at eightfold acceleration as in Fig. 8. Images on the right show the time-varying intensity profiles for one voxel column (**a** and **b**) or row (**c** and **d**), as indicated by the dotted line on the left. The white arrow in (a) points to residual aliasing.

discarded anyway. There were occasionally some faint edge-like artifacts, which were most likely due to residual aliasing of fast moving image features. These artifacts are not obvious from Fig. 8, but their subtle appearance can be noticed more easily, by viewing the images in cine mode or along the time axis (Fig. 9).

Figure 9 shows a further analysis of the in vivo images in Fig. 8. The images on the right show the time-varying intensity profiles for one voxel column (a, b) or row (c, d). For the short-axis *k-t* BLAST images (a), a diagonal striped pattern can be seen at the position of the posterior myocardial wall, as indicated by the white arrow. This was most likely due to residual aliasing. It was not seen in the time-varying intensity profile for *k-t* SENSE. In both short-axis and four-chamber views, the time-varying intensity profiles can be seen to be sharper for *k-t* SENSE. Nevertheless, the images from *k-t* BLAST and *k-t* SENSE are generally in good agreement. The improved sharpness and reduced artifact in *k-t* SENSE match the findings in Ref. 3, since the reconstruction accuracy is expected to improve by incorporating data from additional receiver coils.

DISCUSSION

The image quality of *k-t* BLAST and *k-t* SENSE depends on the signal separation that is achieved inherently by the sampling pattern and by the resolving ability of the reconstruction. As expected, it is increasingly difficult to achieve higher acceleration factors, since more signals have to be packed within the same *x-f* space. Nevertheless, the present work shows that it is possible to minimize image degradation and retain good image quality even at 8× acceleration, by packing the signals in a judicious fashion. In practice, using an unoptimized sampling pattern may still yield acceptable images, since the signal aliasing is still partially resolved. However, there may be increased artifacts in the form of blurring and residual aliasing, which degrade image quality. As mentioned, residual aliasing can often be distinguished from true structural features, since they do not move in a synchronized fashion. Also, these artifacts can be removed by additional filtering, albeit at the expense of losing true object signals. The main impact will be on finer image features, which are usually more difficult to separate due to their lower signals. Therefore, it is advisable and preferable to use an optimized sampling pattern to improve depiction of finer features and the overall reconstruction accuracy.

Optimized sampling patterns are also important for robustness against temporal aperiodicities, such as from arrhythmia. Changes in periodicities result in signal smearing along the temporal frequency axis in *x-f* space. This smearing can potentially increase the amount of signal overlap, as each signal replicate now covers more area in *x-f* space. Optimized sampling patterns improve robustness against aperiodicities by pushing the signal replicates farther apart. As a result, there is more slack region among the replicates, thereby reducing the impact of signal smearing.

In this work, we described a method for optimizing the *k-t* sampling pattern for *k-t* BLAST and *k-t* SENSE. These sampling patterns were optimized to be generally favorable for typical image series, without specific knowledge of the object being imaged. To simplify the optimization

problem, it was assumed that *k*-space was uniformly discretized, and data could only be sampled from the discretized positions. This assumption also simplified the implementation on MR scanners significantly, since the resulting sampling patterns could be implemented using the usual phase encode table. For a given discrete step size, a catalog of optimized sampling patterns could be derived in a straightforward fashion (Fig. 4).

As noted earlier, the discrete step size in *k*-space is in fact arbitrary. So far, for the sake of simplicity, the discrete step size has been set to be the reciprocal of the field of view. This is in line with usual Cartesian sampling. However, it is often not the best choice. For example, it can be seen from Figs. 4 and 5 that sixfold acceleration in 2D is particularly unfavorable, since the sequential interleaved pattern is the only available choice fulfilling the described criteria. However, a net sixfold acceleration can be achieved by other approaches. One approach is to increase the field of view by 7/6 and apply a sevenfold acceleration instead. Another approach is that if there are multiple receiver coils, one may reduce the field of view by 5/6 and apply a fivefold sampling pattern instead. In the latter case, more than one main lobe will be situated at the same temporal frequency, but they can be separated using the additional knowledge of coil sensitivities. In both approaches, it is possible to further separate the main lobes in *x-f* space by using a different field of view together with a different acceleration factor *R*. However, as described earlier, the value of *R* has an impact on the main-lobe separation along the temporal frequency *f* axis and the minimum number of discrete steps. Hence, the best strategy to achieve a net acceleration factor will depend on several experimental considerations, which may make other discrete step sizes possible. These considerations include the number of time frames to acquire and the number and placement of receiver coils. In general, for a given discrete step size, the presented sampling patterns optimize the signal separation for typical image series.

By using *k-t* BLAST and *k-t* SENSE with the optimized sampling patterns, we demonstrated the feasibility of accelerating real-time SSFP imaging significantly. This combination of SSFP and the *k-t* approach is particularly synergistic (18). SSFP yields a much higher baseline SNR compared to spoiled steady-state sequences, so it offers more room for reducing data acquisition, which is always associated with a loss of SNR (19). At the same time, the high acceleration achievable by the *k-t* approach more than overcomes the reduced acquisition efficiency of SSFP, which results from the need to keep TR short to reduce off-resonance effects. However, the straightforward combination of the two leads to unacceptably amplified eddy-current artifacts. These artifacts were reduced to negligible levels by additionally modifying the sweep directions of *k*-space. Thus, by combining the *k-t* approach with SSFP and alternating *k*-space sweeps (9), it was possible to reap the benefits of SSFP (i.e., high SNR and CNR) without compromising the achievable spatial and temporal resolutions.

In this work, the data were reconstructed off-line. Real-time implementation of the reconstruction is also feasible by using short-time Fourier transform to convert between the time *t* and temporal frequency *f* axes (20). At least for the time being, dedicated hardware may be required to handle the computation load in real time. In general, other transforms (i.e., non-Fourier) can also be applied along the temporal axis. In that regard, transforms that are jointly localized in both domains, such as the wavelet transform, favor real-time reconstruction, since the image at a given time point can be reconstructed using only data from nearby time points. The use of alternative transforms will be explored in future work.

In conclusion, we optimized the spatiotemporal sampling pattern in order to separate the image signals more effectively in *x-f* space. By using these optimized sampling patterns with *k-t* BLAST and *k-t* SENSE, it was possible to obtain real-time cardiac SSFP images with an in-plane resolution of approximately 2 mm at more than 25 frames/s.

REFERENCES

1. Madore B, Glover GH, Pelc NJ. UNaliasing by Fourier-encoding the Overlaps using the temporaL Dimension (UNFOLD), applied to cardiac imaging and fMRI. Magn Reson Med 1999;42:813–828.
2. Kellman P, Epstein FH, McVeigh ER. Adaptive sensitivity encoding incorporating temporal filtering (TSENSE). Magn Reson Med 2001;45:846–852.
3. Tsao J, Boesiger P, Pruessmann KP. *k-t* BLAST and *k-t* SENSE: dynamic MRI with high frame rate exploiting spatiotemporal correlations. Magn Reson Med 2003;50:1031–1042.
4. Xiang QS, Henkelman RM. *K*-space description for MR imaging of dynamic objects. Magn Reson Med 1993;29:422–428.
5. Tsao J. On the UNFOLD method. Magn Reson Med 2002;47:202–207.
6. Oppelt A, Graumann R, Barfuss H, Fischer H, Hartl W, Schajor W. FISP: a new fast MRI sequence. Electromedica 1986;54:15–18.
7. Thiele H, Nagel E, Paetsch I, Schnackenburg B, Bornstedt A, Kouwenhoven M, Wahl A, Schuler G, Fleck E. Functional cardiac MR imaging with steady-state free precession (SSFP) significantly improves endocardial border delineation without contrast agents. J Magn Reson Imaging 2001;14:362–367.
8. Haase A, Frahm J, Matthaei D, Hänicke W, Merboldt K. FLASH imaging. Rapid NMR imaging using low flip-angle pulses. J Magn Reson 1986;67:258–266.
9. Jung BA, Hennig J, Scheffler K. Single-breathhold 3D-trueFISP cine cardiac imaging. Magn Reson Med 2002;48:921–925.
10. Willis NP, Bresler Y. Lattice-theoretic analysis of time-sequential sampling of spatiotemporal signals—Part I. IEEE Trans Inform Theory 1997;43:190–207.
11. Willis NP, Bresler Y. Lattice-theoretic analysis of time-sequential sampling of spatiotemporal signals—Part II: Large space-bandwidth product asymptotics. IEEE Trans Inform Theory 1997;43:208–220.
12. Edelstein WA, Hutchison JM, Johnson G, Redpath T. Spin warp NMR imaging and applications to human whole-body imaging. Phys Med Biol 1980;25:751–756.
13. Fuderer M. The information content of MR images. IEEE Trans Med Imaging 1988;7:368–380.
14. Doyle M, Walsh EG, Blackwell GG, Pohost GM. Block regional interpolation scheme for k-space (BRISK): a rapid cardiac imaging technique. Magn Reson Med 1995;33:163–170.
15. Pruessmann KP, Weiger M, Scheidegger MB, Boesiger P. SENSE: sensitivity encoding for fast MRI. Magn Reson Med 1999;42:952–962.
16. Hansen MS, Kozerke S, Pruessmann KP, Boesiger P, Pedersen EM, Tsao J. On the influence of training data quality in *k-t* BLAST reconstruction. Magn Reson Med 2004;52:1175–1183.
17. Conway JH, Sloane NJA. Sphere packing, lattices and groups. New York: Springer-Verlag; 1999. 703 p.
18. Kozerke S, Tsao J, Razavi R, Boesiger P. Accelerating cardiac cine 3D imaging using *k-t* BLAST. Magn Reson Med 2004;52:19–26.
19. Pohmann R, von Kienlin M, Haase A. Theoretical evaluation and comparison of fast chemical shift imaging methods. J Magn Reson 1997;129:145–160.
20. Tsao J, Kozerke S, Hansen M, Eggers H, Boesiger P, Pruessmann K. Moving-buffer *k-t* BLAST for real-time reconstruction: Cartesian & simplified radial cases. In: Proceedings of the 12th Annual Meeting of ISMRM, Kyoto, Japan, 2004. p 635.